We are IntechOpen, the world's leading publisher of Open Access books Built by scientists, for scientists

6,900
Open access books available

186,000
International authors and editors

200M
Downloads

Our authors are among the

154
Countries delivered to

TOP 1%
most cited scientists

12.2%
Contributors from top 500 universities

CLARIVATE ANALYTICS
BOOK CITATION INDEX
INDEXED

WEB OF SCIENCE™

Selection of our books indexed in the Book Citation Index
in Web of Science™ Core Collection (BKCI)

Interested in publishing with us?
Contact book.department@intechopen.com

Numbers displayed above are based on latest data collected.
For more information visit www.intechopen.com

Studies of Lithium-Oxygen Battery Electrodes by Energy-Dependent Full-Field Transmission Soft X-Ray Microscopy

Dino Tonti, Mara Olivares-Marín,
Andrea Sorrentino and Eva Pereiro

Additional information is available at the end of the chapter

Abstract

Energy-dependent full-field transmission soft X-ray microscopy is a powerful technique that provides chemical information with spatial resolution at the nanoscale. Oxygen K-level transitions can be optimally detected, and we used this technique to study the discharge products of lithium-oxygen batteries, where this element undergoes a complex chemistry, involving at least three different oxidation states and formation of nanostructured deposits. We unambiguously demonstrated the presence of significant amounts of superoxide forming a composite with peroxide, and secondary products such as carbonates or hydroxide. In this chapter, we describe the technique from the fundamental to the observation of discharged electrodes to illustrate how this tool can help obtaining a more comprehensive view of the phenomena taking place in metal air batteries and any system involving nanomaterials with a complex chemistry.

Keywords: metal-air batteries, superoxide, peroxide, XAS, XANES, TXM, spectromicroscopy

1. Introduction

With lithium ion batteries becoming a mature technology, it is now clear that applications such as electric vehicles require chemistries with higher energy density to reach acceptable driving ranges without compromising performance and comfort already common with conventional vehicles. This pushed high research efforts in the area of lithium-air (or more precisely lithium-oxygen) batteries, presenting the highest energy density among known scalable battery devices, and of metal-air batteries in general. However, the difficulty to obtain a

high reversibility and long cycle life still implies a significant barrier to become a technology. In many applications the precise knowledge of composition and morphology of materials at the nanoscale is a key to control performance and reliability. Metal-oxygen batteries are one of these cases; in fact, they involve complex reaction and precipitation processes that need to be understood in detail to obtain true reversible operation. The determination of composition as a function of position in the nano-sized precipitate at different charging states is the most valuable information for this understanding. A few physical techniques are routinely used to reveal the processes underlying battery behavior, e.g., XRD, TEM, SEM, XPS, FTIR, Raman, and mass spectroscopy. In this chapter we present the application to this problem of energy-dependent full-field transmission soft X-ray microscopy. This spectromicroscopical technique based on synchrotron radiation is able to give a full picture at the nanometer scale of the oxidation state and spatial distribution in the cathode of oxygen, the most relevant element in any metal-air battery. Although a host of physical techniques are routinely used to reveal the processes underlying battery behavior (e.g., XRD, TEM, SEM, XPS, FTIR, Raman, and mass spectroscopy), this technique is unique in providing high-resolution imaging with chemical information.

We will first introduce the basic concepts of metal-air batteries and transmission X-ray micros-copy, then detail how the technique can be applied to battery electrodes, and finally provide some examples of studies that we performed on lithium-oxygen cathodes, which can be easily extended to other metal-air systems and all those materials where oxygen redox reactivity is involved.

2. Metal-air batteries and the nature of discharge products

With lithium ion batteries becoming a mature technology, it is now clear that applications such as electric vehicles require chemistries with higher energy density to reach accept-able driving ranges without compromising performance and comfort already common with conventional vehicles. This pushed high research efforts in the area of lithium-air (or more precisely lithium-oxygen) batteries, presenting the highest energy density among known scalable battery devices, and of metal-air batteries in general. However, the difficulty to obtain a high reversibility and long cycle life still implies a significant barrier to become a technology. Compared to conventional lithium-ion batteries the reversibility and cycle life of metal-air batteries is generally frustrating [1]. While in a lithium-ion battery the main process is essentially ion transport through different phases that essentially leave electrode interfaces unaffected, in metal-air batteries reversible electrodeposition processes have to take place at the electrodes. For instance, with a lithium anode and aprotic electrolytes molecular oxygen is reduced and precipitates as insulating lithium peroxide inside a porous carbonaceous cathode [2]:

$$\text{Anode:} 2\,Li \;\rightarrow\; 2\,Li^+ + 2\,e^-$$
$$\text{Cathode:} O_2 + 2\,Li^+ + 2\,e^- \;\rightarrow\; Li_2O_2\!\downarrow$$
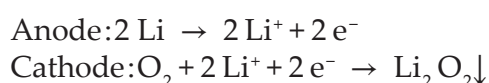
The latter reaction may proceed through two subsequent one-electron oxygen reduction steps or through chemical disproportionation of electrochemically generated superoxide:

$$Li^+ + O_2 + e^- \rightarrow LiO_2$$

$$2\,LiO_2 \rightarrow Li_2O_2\downarrow + O_2$$
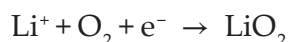
This implies problems of controlling nucleation and growth processes, but more importantly the oxygen chemistry hugely increases complexity and triggers parasitic reactions with the organic electrolyte and with both electrodes [3, 4].

However, the control of texture, composition, and crystallinity of the discharge products can also have important consequences on the capacity, rate capability, and reversibility. In fact, capacity directly depends on the discharged peroxide volume, which depending on its morphology can be more or less well distributed in a given porous network before it becomes clogged or passivated [5]. The size of the precipitate particles also affects rechargeability: conditions that favor deposition of smaller particles obtain better reversibility [6, 7], likely for the more favorable surface-to-volume ratio. Evidence of the reaction intermediate superoxide in the precipitate has been reported [8–11] and it has been demonstrated that this is easier to oxidize than peroxide [12]. In effect Na/O_2 and K/O_2 cells, where superoxide prevails, have remarkably higher reversibility than Li/O_2 [13, 14].

A precise characterization of the nature and the evolution of the discharge products, and in particular the oxidation state of oxygen, is therefore essential to understand the processes underlying the electrochemical behavior of the cell, and can lead to improvements in materials and operating conditions. Given the light elements involved and the poor stability of incompletely reduced Li-O compounds many imaging, spectroscopic, or diffraction techniques are not suitable for their compositional analysis. In addition, amorphous phases are occasionally possible with Li_2O_2 (which may benefit rechargeability) [15] and usual with Li superoxide [10]. It is then evident that a technique such as full-field transmission spectromicroscopy has high value, being able to accurately spatially resolve distributions of superoxide, peroxide, and other oxygen compounds even within a single particle, and regardless of crystallinity.

3. Full-field transmission soft X-ray spectromicroscopy

In this paragraph the full-field transmission spectromicroscopy technique will be shortly explained. In Section 3.1, some basic concepts will be introduced following references [16, 17]. Then two possible experimental setups, the scanning and the full-field X-ray transmission microscope will be compared [16]. Finally, a brief paragraph will describe the full-field transmission microscope installed at the Mistral beamline (Alba Light Source, Spain) [18, 19].

3.1. The interaction of X-rays with matter

Usually for X-rays, the refraction index is written as:

$$n(\omega) = 1 - \delta(\omega) - i\beta(\omega) \tag{1}$$

while $E = \hbar\omega$ is the energy of the incident radiation. It is interesting to consider the asymptotic trend of δ and β for high energy (E far from absorption edges):

$$\delta(E) \propto \frac{1}{E^2} \quad \beta(E) \propto \frac{1}{E^4} \tag{2}$$

Let us consider now the propagation of a plane wave in the sample. Assuming $\mathbf{kr} = kr$ and using the *dispersion relation* $k^2 = \omega^2 n^2/c^2$, one has:

$$\mathbf{E}_0\, e^{i(\omega t - kr)} = \mathbf{E}_0\, e^{i[\omega t - \frac{\omega}{c}(1-\delta-i\beta)r]} = \mathbf{E}_0\, e^{i(\omega t - k_0 r)}\, e^{ik_0\delta r}\, e^{-k_0\beta r} \tag{3}$$

where $k_0 = \omega/c = 2\pi/\lambda$ is the wave vector in vacuum. In Eq. (3), the first factor is the phase advance had the wave been propagating in vacuum; the second factor containing δ represents the modified phase shift due to the interaction with the medium; and the last factor containing β represents the decay of the wave amplitude in the medium due essentially to photoelectron absorption for X-rays. Hence, the phase shift due to the interaction with the sample is determined by δ, while the attenuation by β. The *linear absorption coefficient* μ is defined as the inverse of the distance into the material for which the intensity related to the wave amplitude, Eq. (3), is diminished by a factor $1/e$. Using Eq. (3):

$$\mu(E) = \frac{4\pi}{\lambda}\beta(E) \tag{4}$$

It is usually measured in μm^{-1} and the corresponding characteristic distance is called the *attenuation length*. μ is a rapidly increasing function of the atomic number and a rapidly decreasing function of the energy, taking into account Eq. (2):

$$\mu(E) \propto \frac{1}{E^3} \tag{5}$$

and at some particular energies called "absorption edges" it has peaks that correspond to the energies required to eject an electron from an internal core level to a final available electronic state. It is useful to introduce the *mass absorption coefficient*, defined as

$$\mu_m = \frac{\mu}{\rho} \tag{6}$$

with ρ being the mass density, $\rho = m_a n_a$ (m_a is the atomic mass, n_a is the density of the atoms).

To properly account for the transitions corresponding to the absorption edges, the use of quantum mechanics is needed. Considering a well-defined initial core state and using the *Fermi golden rule* in the *dipole approximation* one can write μ_m as:

$$\mu_m(E) \propto \left| \langle \psi_i | \hat{\varepsilon} \cdot r | \psi_f \rangle \right|^2 \rho_f(E_f) \tag{7}$$

where ψ_i and ψ_f are the initial and final single electron states, E_i and E_f are the corresponding energies and $E = E_f - E_i$ is the energy of the incident photons, ρ_f the density of final state, and $\hat{\varepsilon}$ the polarization of the electric field. The interaction between the atom and the electromagnetic field, classically pictured by the wave in Eq. (3), removes an X-ray photon whose energy is used to promote an electron from the initial core state ψ_i to the final state ψ_f. The absorption is modulated by the density of final state which has peaks in correspondence of the absorption edges. The dipole matrix element, almost flat with the energy, contains the angular momentum selection rules for dipole transitions (l = orbital angular momentum, s = spin, j = total angular momentum, m = z-component of the total angular momentum):

$$\Delta 1 = \pm 1, \quad \Delta s = 0, \quad \Delta j = \pm 1, 0, \quad \Delta m = 0 \tag{8}$$

and the dependence on the direction of the photon polarization $\hat{\varepsilon}$.

X-ray absorption imaging technique consists in detecting the photons transmitted through the observed object. Experimentally, the number of photons N after the transmission through the sample, along z, obeys to the *Beer-Lambert's law*:

$$N(x, y) = N_0(x, y) \exp \left[-\int_{\text{sample}} \mu(x, y, z)\, dz \right] \tag{9}$$

where N and N_0 are the emerging and incident number of photons, respectively, and the integral is extended through all the sample thickness. The measured transmission $T = I/I_0$ (with I and I_0 proportional to N and N_0, respectively) depends exponentially on the linear absorption coefficient μ, integrated along the X-ray path in the sample (**Figure 1**).

In a transmission microscope based on X-ray photons, the contrast will therefore depend on the sample thickness, the elements by which it is composed, their density, and the energy and polarization of the incident radiation. Assuming not oriented samples (so that we neglect the polarization) and μ constant along z in a thickness t, we can write:

$$\mu(x, y, E)\, t = \mu_m(x, y, E)\, \rho t = -\ln \left(\frac{I}{I_0} \right) \tag{10}$$

This product is proportional to the *absorbance A*, which is defined as $A = -\log_{10}(I/I_0)$, and is usually considered in the place of the transmission because of its additivity:

$$\mu t = \sum_i \mu_i t_i \tag{11}$$

Figure 1. Optical absorption and the Beer-Lambert's law.

which, for the particular case of i chemical species in a thickness t, becomes:

$$\mu t = t \sum_i \mu_{m,i} \rho_i \tag{12}$$

As a function of the photon energy parts of the images will then suddenly become darker (or brighter if we use the absorbance) when the radiation is triggering some electronic transitions allowed by Eqs. (7) and (8). As the exact energy is also dependent on the atom environment, it will also be possible to detect chemical states of the same element. This chemical information is available with spatial resolution down to few tens of nanometers in a synchrotron-based transmission X-ray microscope and the corresponding technique is called transmission X-ray spectromicroscopy. By using X-rays of the "soft" energy region (<3 KeV), it is possible to access transitions from core levels of light elements, among them the K-edge of nitrogen, oxygen, fluorine, as well as L – and M - edges of other elements (**Figure 2**).
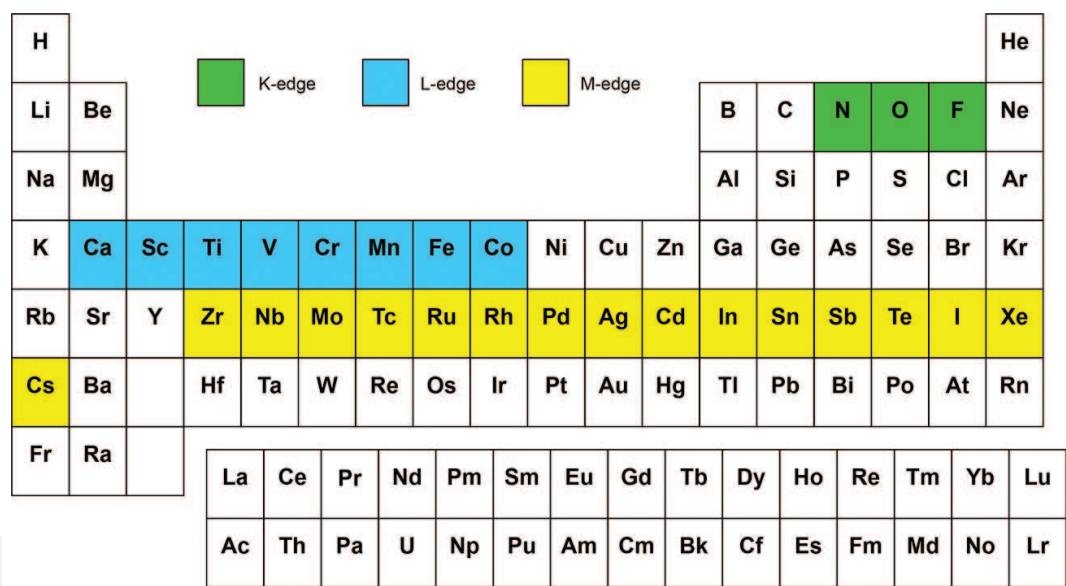

Figure 2. Accessible absorption edges with a soft X-ray radiation of 300–800 eV in the periodic table.

3.2. Zone plate-based X-ray transmission microscopes

Using the "radiography setup" depicted in **Figure 1**, the spatial resolution would be limited by the detector pixel size to few microns. In lens-based microscopy, this limit is imposed by the lenses. In the following we will briefly describe two examples of lens-based microscope geometries used at synchrotron radiation sources: the full-field transmission X-ray microscope (TXM) and the scanning transmission X-ray microscope (STXM), both represented in **Figure 3**.
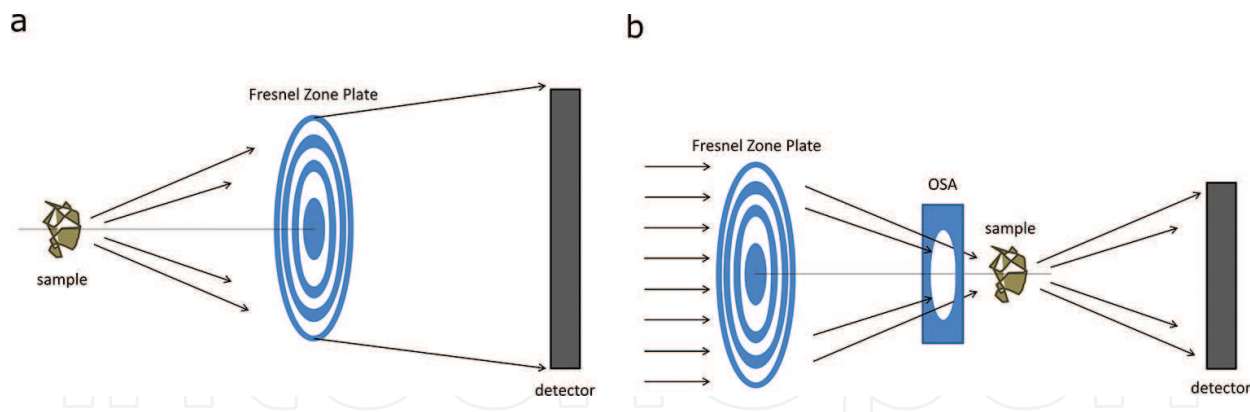
Figure 3. Scheme of the two common transmission X-ray microscopes: (a) Full-field microscope, in which a full sample image is formed on the detector; (b) Scanning microscope, in which the sample is scanned in the focal spot of the incoming beam.

Both of them are lens microscopes based on the application of Fresnel Zone Plate diffractive lenses (ZP). A ZP lens works like a circular diffraction grating whose period radially decreases from the center in such a way that all the waves of the same diffracted order are redirected to the same point (**Figure 4**). The expression for the focal length can be calculated as:

$$f \cong \frac{4N(\varDelta r)^2}{\lambda}$$
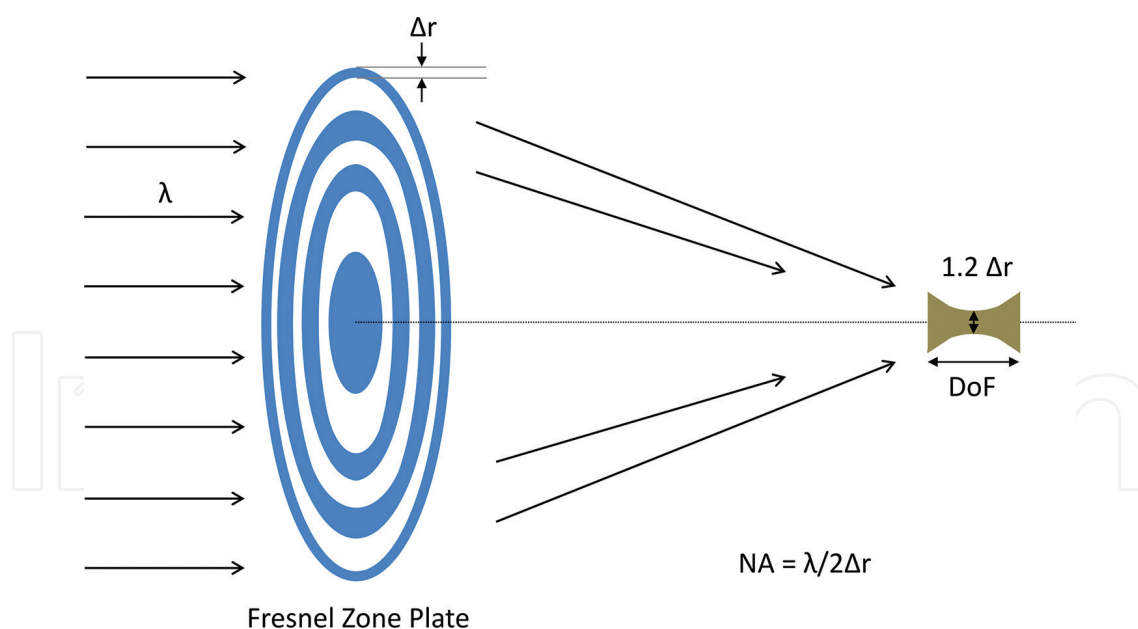
(13)

Figure 4. Conceptual scheme of a Fresnel Zone Plate lens.

Present technology allows the fabrication of ZP capable to produce focal spots down to few tens of nanometers (≥15 nm) [20]. Spatial resolution (r_s) and depth of focus (DoF) both depend

on λ and the *numerical aperture* (NA) of the lens which is, in the case of ZP lenses, related to the dimension of the outermost zone width Δr:

$$r_s = \frac{0.61\lambda}{NA} = 1.22\Delta r \quad DoF = \pm\frac{1}{2}\frac{\lambda}{(NA)^2} = \pm\frac{2(\Delta r)^2}{\lambda} \tag{14}$$

In the first equation of (14) the spatial resolution is defined following the *Rayleigh* criterion. It is interesting to note that a better spatial resolution will imply also a smaller DoF.

The nanofabrication of a ZP is typically realized on a thin silicon nitride membrane and involves high technology processes such as electron beam lithography. In general, the choice of the material for the ZP's opaque zones determines the efficiency depending on the energy range. For the TXM case we have the typical scheme of a common visible light microscope: a sample is placed at the focal plane of two lenses. The first lens is usually called "condenser" and it focalizes the beam on to the sample plane, while the second lens is called "objective lens" and it produces a full magnified image of the sample on to the detector plane. The objective lens is a ZP lens which works as a *thin lens* between the sample and the detector plane so that the magnification M is:

$$M = \frac{p}{q} \tag{15}$$

With p being the distance ZP-detector and q being the distance ZP-sample as indicated in **Figure 5**.
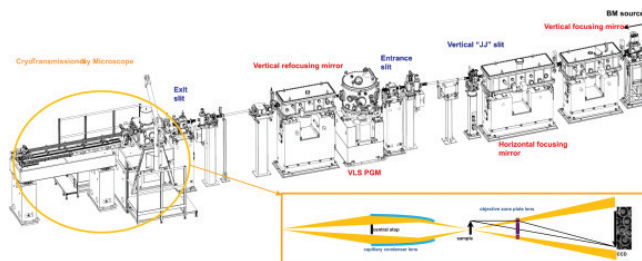

Figure 5. Mistral beamline layout. In the inset, a scheme of the TXM optics setup is reported.

The spatial resolution is limited by the NA of the objective lens, i.e., by the external zone width of the ZP lens as indicated in Eq. (14). This limit is reached if the microscope operates at M big enough to neglect the dimension of the pixels size of the detector (typically a CCD-based detector) and if the NA of the objective lens is filled by the beam emerging from the sample. Also, the ZP lens is strongly chromatic as indicated by Eq. (13), so that also a minimal requirement on the energy resolution of the incident beam has to be satisfied: $\Delta\lambda/\lambda \leq 1/N$, with N being the number of zones.

In a STXM system, the sample is placed in the focal spot of a ZP lenses. If illuminated with the proper coherent beam the ZP will produce a focal spot (more precisely an *airy pattern*) with

resolution set again by the first equation of (14). In this case, higher order diffracted beams will be stopped using an order sorting aperture (OSA) as indicated in **Figure 3**. The sample is scanned through the ZP focal spot and the full image of the sample is reconstructed electronically, step by step. The spatial resolution will be limited by the dimension of the focal spot produced by the ZP on the sample. **Table 1** summarizes the main properties of the two microscopes.

TXM	STXM
Best spatial resolution	Good spatial resolution
Shortest exposure time	Longer exposure time
Higher radiation dose	Least radiation dose
	Requires spatially coherent radiation

Table 1. Comparison between the main properties of full-field and scanning transmission electron microscopy.

The main advantage of the STXM over the TXM system is in terms of radiation dose: the lens is before the sample and then all the photons emerging from the sample are used to produce the image. Instead in a TXM system, the ZP is after the sample: due to its limited efficiency, most of the photons arising from the sample will not contribute to the formation of the image, therefore to obtain the same image quality of a STXM, the TXM will require more radiation dose absorbed by the sample. The main advantage of the TXM over the STXM system is in terms of the exposure time: in one "snapshot" the full image of the sample is obtained.

3.3. The MISTRAL microscope

An example of a state-of-the-art soft X-ray full-field transmission microscope is the one installed at the Mistral beamline of the ALBA Light source. A picture of the beamline (BL) is reported in **Figure 5**. The BL is devoted to transmission cryotomography of biological cells in the water window energy range (284.2–543.1 eV [21]). It is useful to distinguish between the BL optical elements and the TXM which is just the end station of the BL, as indicated in the picture. Presently the TXM can works in the energy range (ER) between the C–K edge and the Ni L edge excluded, i.e., 290–850 eV. All the optical elements before the TXM work to prepare the beam for the condenser lens of the microscope and are in ultra-high vacuum chambers (working p ~1×10^{-9} mbar) to minimize absorption and scattering of the X-ray beam. Moreover, the full beamline from the source to the CCD detector chip is windowless. In the case of Mistral the condenser lens is a glass capillary which work like a single reflection elliptical mirror. It is characterized by a good efficiency (50–75% in the ER) and achromaticity: its focal length of about 1 cm is energy independent. The 2×2 μm^2 condenser focal spot is wobbled to cover a field of view of typically 10×10–16×16 μm^2 on the sample plane. Two ZP are available as objective lens: 25 and 40 nm ZP. The first one is used typically for experiments

in which one wants to maximize the 2D spatial resolution and the depth of focus is not a critical parameter. More technical details on the MISTRAL beamline are reported in references [18, 19].

4. Spectromicroscopy at the O K-edge of discharged cathodes

In this section, we describe the preparation, collection, and analysis of cathodes used in Li-oxygen batteries, although most of the principles and considerations may well apply to other systems and energy regions.

4.1. Sample preparation and transfer

For images of optimal quality, we take common carbon-coated Au TEM grids (200 mesh, 3.05 mm diameter) directly as a cathode. Gold works as a current collector that is inert in the cathode electrochemical window, while carbon provides an ideal substrate for transmission microscopy. However, also a few micrograms of super P/PVdF slurry are deposited on the TEM grids to provide a roughened surface closer to that present in practical electrodes.

Electrochemical treatments are performed using homemade cell based on the Giessen battery design [13], resulting in Swagelok-like battery arrangement. After the electrochemical treatment the cell is opened in an Ar-filled glove box and the grid washed with DME and hexane to fully remove the electrolyte. The grid is then transferred in the microscope in cryogenic condition ($T < 110$ K) under N_2 vapor to minimize atmospheric contamination. The samples are kept at cryogenic temperature and under high vacuum during the measurements.

4.2. Measurement protocol

Selection of a field of view consists of two steps, first an overview of the TEM mesh with a visible light microscope (VLM), and then selection of a specific mesh hole where a 100 μm × 100 μm mosaic image can be composed by 10 × 10 individual TXM images (see **Figure 6**). Repeating mosaics at two energies, above and below the O K-edge can be useful for a first localization of oxygen compounds.

For the case of the O K level, XANES images are collected varying the incident photon energy with an exposure time of 2 s at each energy step. For each energy step, a flat field image (FF), i.e., an image without the sample, is recorded. An energy range of 515–580 eV ensures the most reliable spectral normalization and allows EXAFS analysis. The energy step can be adjusted between 0.1 and 0.5 eV depending on the spectral features to record. The objective zone plate lens (outermost zone width of 40 nm, 937 zones) and the CCD detector positions are automatically adjusted to maintain focus and constant magnification. The CCD motion is the slowest part of acquisition which typically requires between 1 and 2 h.
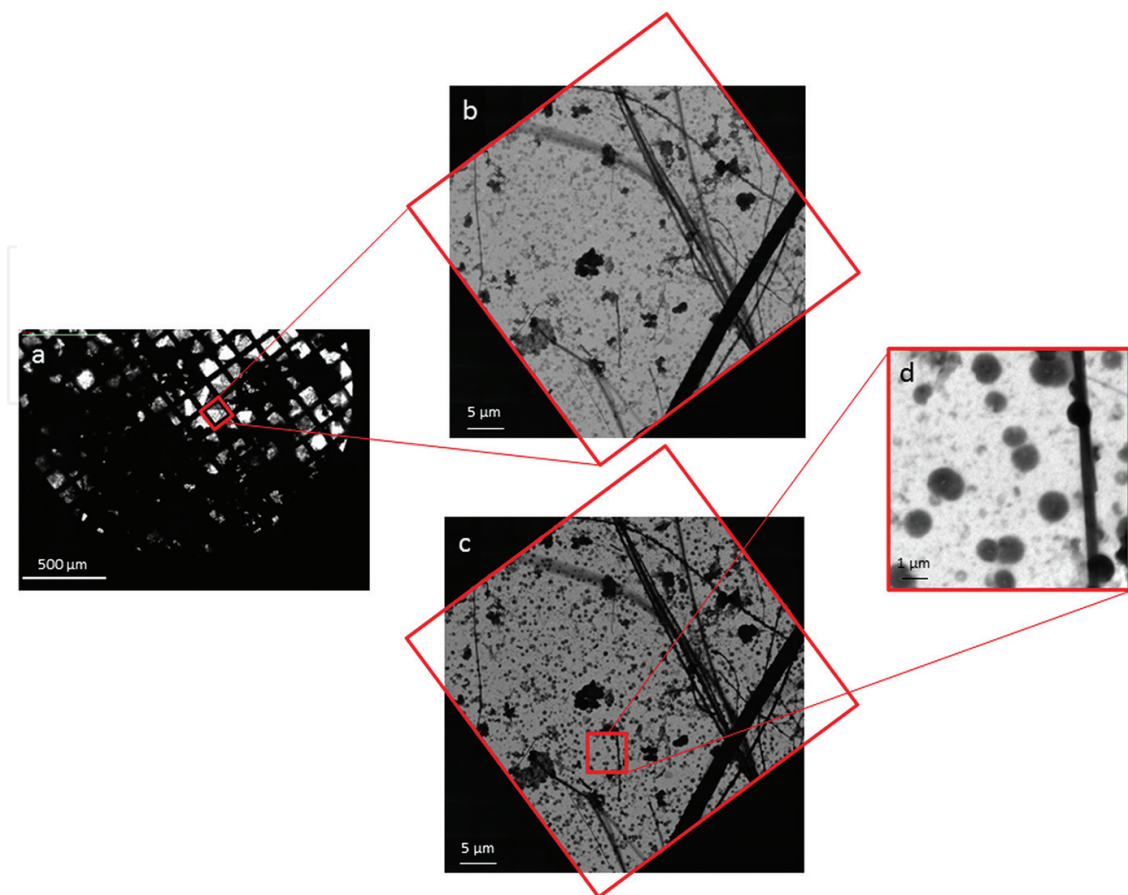
Figure 6. Stepwise selection of a field of view: grid overview by VLM (a), mosaic TXM image of an individual mesh hole before (b) and after (c) the O-K edge, and TXM field of view (d).

4.3. Radiation damage

A recurring issue in techniques involving high brilliance light is the sample stability to irradiation. This is often considered a major problem with organic compounds, whereas inorganic compounds are regarded as essentially stable [22]. However, Li_2O_2 is also very sensitive. For instance, in our own experience, electron microscopy requires special care, as the electron beam is able to fully decompose a micrometric layer of lithium peroxide in a few seconds, as shown in **Figure 7**.

Qiao et al. [24] specifically studied the effect of irradiating lithium peroxide, oxide, and carbonate with soft X-rays at room temperature. They found that carbonate and peroxide evolve toward oxide within several minutes of irradiation. In contrast with their respective electrochemical oxidation stability, the evolution of carbonate is faster, with oxide features appearing after 1 h for peroxide and already after 20 min for carbonate. The stability of a given compound depends on the activation process. However, in general, the high cross-section of soft X-rays implies a stronger interaction with matter and consequently a faster degradation than hard X-rays, in particular when the photon energy is close above the absorption edge of elements such as C and O.
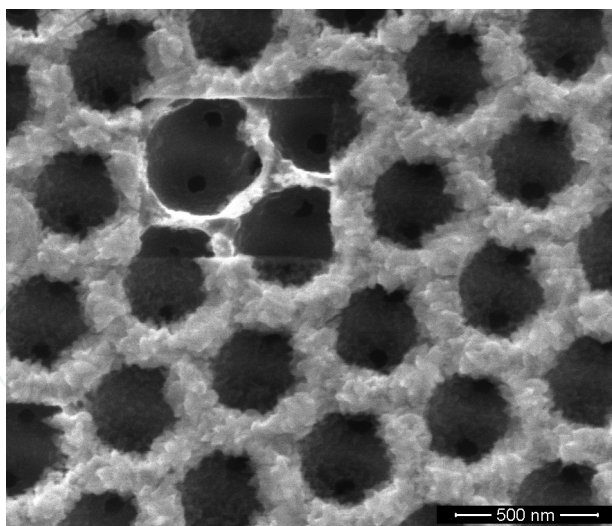
Figure 7. SEM image showing the effect of the electron beam on the deposits of a Li/O$_2$ discharged cathode. The support is a carbonaceous inverse opal [23]. The deposit-free rectangle has been obtained after scanning during about 1 min for a higher magnification image.

This problem is obviously of special relevance for biologic samples, which are always observed with soft X-rays in cryogenic conditions. The lower nuclear thermal motion favors the reconstruction of the bonds excited by radiation, significantly improving the sample stability. For this reason, we also keep our discharged electrodes at $T < 110$ K (liquid nitrogen) during irradiation with soft X-rays. Under these conditions, we can irradiate long enough to gain acceptable signal to noise and energy step without evident damage. As an example, **Figure 8** compares two O K-edge XANES spectra (duration about 2 h each) of a sample recorded before (red) and after 24-h period (blue). Spectra demonstrate very good reproducibility corresponding to no detectable radiation damage within our resolution and experimental noise.

4.4. Reference samples

Reference samples are essential for correct assignment of the peaks found in the sample. They must be measured in the same conditions and preferably in the same session to allow similar instrumental peak broadening and proper spectra subtraction. This is useful to detect components that may be masked by more abundant species.

Unfortunately, commercial compounds may not always correspond exactly to the expected composition. Although also commercially available, we have chemically generated Li$_2$O$_2$ from the reaction of KO$_2$ with dicyclohexyl-18-crown-6 (crown ether) in solution [25]. We have obtained images of the precipitate with different local O K-edge XANES spectra. By inspection of the spectra at different points of the images we concluded that locally rather pure phases of both Li$_2$O$_2$ and Li$_2$CO$_3$ coexisted, being the first in agreement with the literature [24], and the second with a commercial sample we measured. LiO$_2$ can only be hardly obtained in a pure
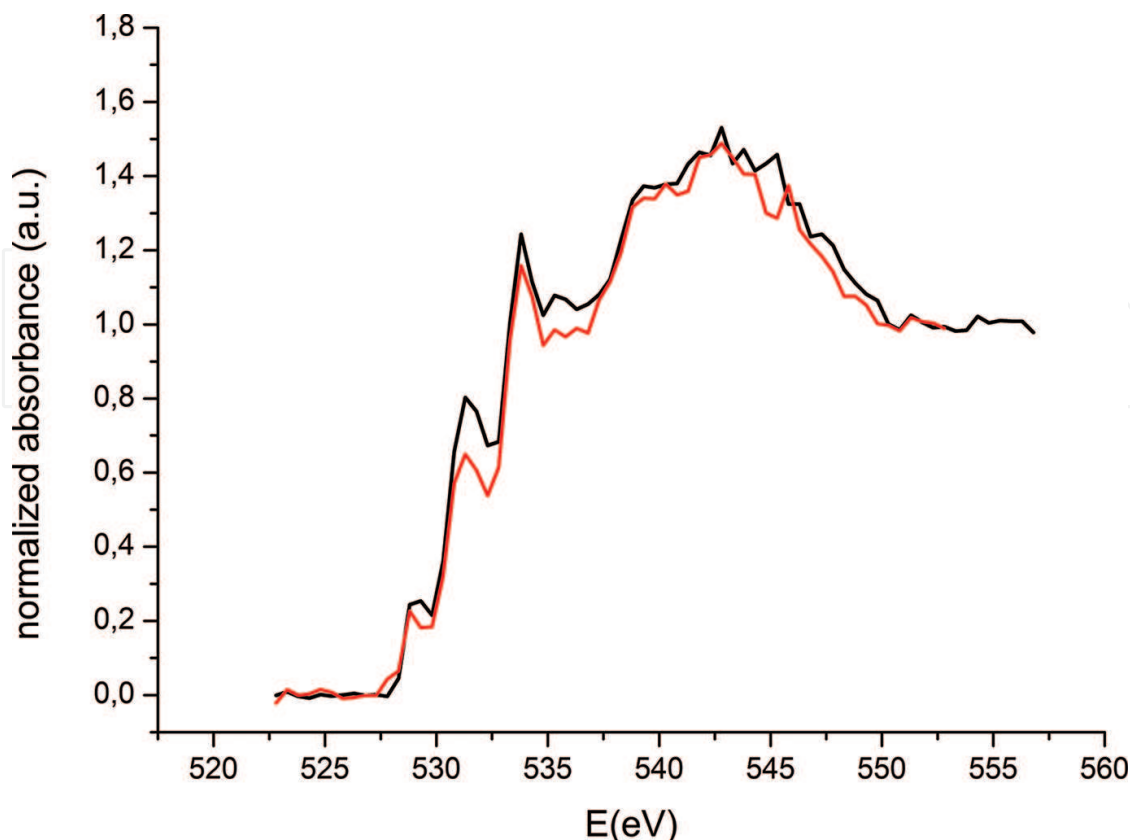
Figure 8. O K-edge XANES spectra of discharged sample before (black) and after (red) 24-h in the same experimental condition. Reprinted with permission from Olivares-Marín et al. [11]. Copyright 2015 American Chemical Society.

form [12, 26], and we used just a literature absorption spectrum as reference [26], mainly to confirm its energy.

4.5. Data analysis

4.5.1. Images normalization, alignment, and spectra extraction

As a first step, each image of the energy scan is normalized to one using the corresponding FF. This normalization consists in simply dividing the image with the sample by the corresponding FF, obtaining the transmission $T = I/I_0$ as a function of the energy (see Section 3.1). In the transmission only, the measured intensity variations along the energy scan due to the sample itself are taken into account, all the contribution coming from the optical setup (beamline and microscope optics) are discarded. The normalized images (or transmission images) present drifts along the scan due to the relative movement between the ZP lens and the CCD detector. Therefore, the image sequence needs to be aligned. At Mistral for instance this is done using a in-house software named "ctalign." Each of the images is aligned taking as reference a chosen ROI of the first image of the scan. The software uses the normalized cross-correlation of both ROIs to detect the best matching between them. Once aligned, the absorbance images can be simply obtained from the corresponding transmission images using Eq. (10), i.e., calculating

the –log of the series. The free NIH ImageJ software [27] is for instance useful to handle the aligned TXM images and doing calculations with them.

By taking the average absorbance from a given region of an image for all images, the absorption spectrum for that region is obtained. In principle, the technique gives access to a single pixel spectra analysis, practically the dimension of the selected region is limited by the lens resolution, the effectiveness of the series alignment, and single pixel spectra noise to 5–6 pixels^2.

4.5.2. Spatial distribution of the discharge products

Given that the different oxygen reduction states present in discharged metal/oxygen electrodes (superoxide, peroxide, and carbonate) are characterized by distinct absorption peak energies (around 529, 531, and 533 eV, respectively) oxygen-state-resolved maps can be obtained. A full quantitative approach consists in measuring a full set of pure reference samples (superoxide, peroxide, and carbonate in our case) and fit with them the obtained measured spectra. If measured reference spectra are not available some sophisticated linear algebra technique such as principle component analysis and factor analysis can also be used for the interpretation of XANES spectra. The number of principal components determined in this way was used as the basis for multivariate curve resolution-alternating least squares (MCR-ALS) analysis [28]. However, precise and accurate calculations of all spectral features are still difficult and not always reliable. Presently, quantitative analyses of XANES spectra using *ab initio* calculations are very rare, and a full description of absorption spectra data analysis and interpretation is beyond the scope of this paragraph. Here, we will describe a simple, qualitative/semiquantitative approach based on the construction of absorbance image differences D obtained from single absorbance images at specific energies. Let us consider two chemical species A and B in a thickness t, then the corresponding absorbance will be (from Eq. 12):

$$\mu(E)\, t = (\mu_{m,A}(E)\, \rho_A + \mu_{m,B}(E)\, \rho_B)\, t \tag{16}$$

where $\mu(E)\, t$ represents the intensity map in the absorbance image at a generic energy E. Now if we choose the two values of the energy position of the absorption edge peak maximum and minimum, respectively, of the species A for instance ($E_{\mathrm{MAX,A}}$ and $E_{\mathrm{min,A}}$ in **Figure 9**), we can write for the corresponding absorbance difference D_A

$$D_A = (\mu_{m,A}(E_{\mathrm{MAX,A}})\, \rho_A + \mu_{m,B}(E_{\mathrm{MAX,A}})\, \rho_B - \mu_{m,A}(E_{\mathrm{min,A}})\, \rho_A - \mu_{m,B}(E_{\mathrm{min,A}})\, \rho_B)\, t \tag{17}$$

$$\text{and assuming } \mu_{m,B}(E_{\mathrm{MAX,A}}) \approx \mu_{m,B}(E_{\mathrm{min,A}}), \tag{18}$$

$$D_A \approx (\mu_{m,A}(E_{\mathrm{MAX,A}}) - \mu_{m,A}(E_{\mathrm{min,A}}))\rho_A\, t \tag{19}$$

If $\mu_{m,A}(E_{\mathrm{min,A}}) \ll \mu_{m,A}(E_{\mathrm{MAX,A}}) \Rightarrow D_A \approx \mu_{m,A}(E_{\mathrm{MAX,A}})\rho_A t$, that is the absorbance image difference D_A is proportional to the concentration map of the chemical specie A. Doing the same for the specie B, we have:
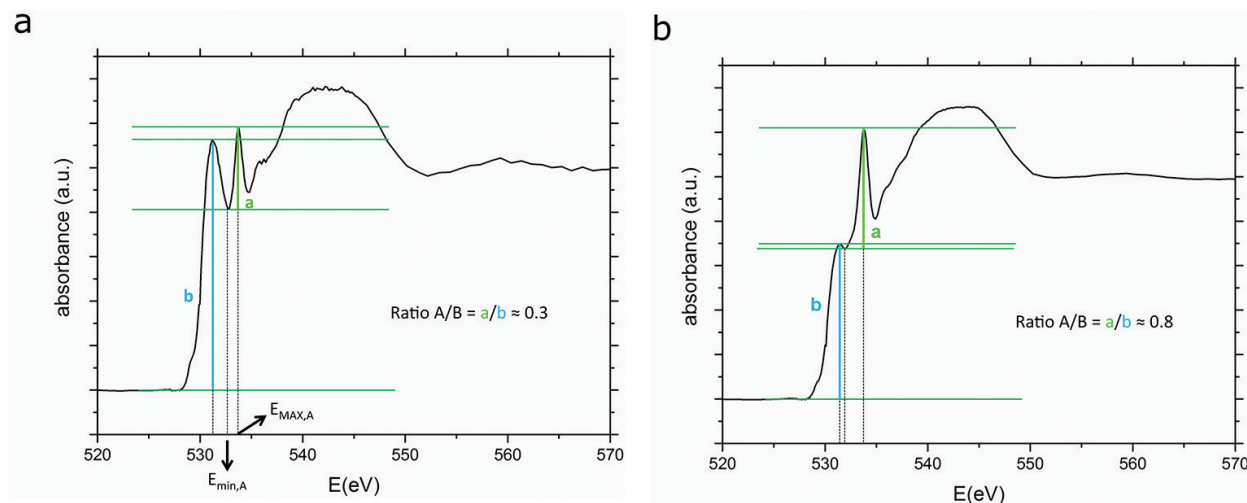
Figure 9. Two examples of fraction estimation for different components in integrated spectra.

$$D_B \approx \mu_{m,B}(E_{MAX,B}) \rho_B t \qquad (20)$$

and then for the ratio between the two species: $\frac{D_A}{D_B} \propto \frac{\rho_A}{\rho_B}$. The corresponding estimation in integrated spectra is shown in **Figure 9**.

Under these considerations we have used absorbance images corresponding to the relative maximum absorbance of LiO_2 (528.75 eV), Li_2O_2 (531.25 eV), and Li_2CO_3 (533.8 eV). The image at 520 eV was subtracted from that at 528.75 eV to obtain the 2D LiO_2 distribution, and the image at 528.75 eV was subtracted from that at 531.25 eV to obtain the one for Li_2O_2. Also, Li_2CO_3 was calculated subtracting image at 531.25 eV minus image at 533.8 eV. Three distribution images obtained were then merged with different colors.

From these maps and possibly calibrating the image intensity using reference samples with known ratio between species, it is possible to obtain profiles or images of ratios and fractions, which is useful to establish correlations or associations between species.

5. Some case studies

Thanks to the measurement and analysis procedure described above, synchrotron-based energy-dependent transmission soft X-ray microscopy (TXM) provides a unique access to the chemical state, spatial distribution, and morphology of oxygen-containing materials in particular when they present different oxidation states, regardless of their crystalline state. Given its lateral resolution, this technique is also able to reveal minor components that are not evident in the integrated spectra, but are well localized. In this part we will illustrate the potential of this technique with some examples of energy-dependent TXM measurements on cathodes discharged in Li/O_2 cells. In fact, this allows detecting different oxygen-bearing components among the discharge products of electrodes, and associating it to its characteristic shape. In this way it is possible to quantify and localize the distribution of the oxygen discharge products, revealing lithium superoxide, peroxide, hydroxide, and carbonates.

5.1. Spatial distribution of products

The discharge products of Li/O$_2$ batteries are reported in the literature with different morphology and composition. When the product is well crystalline electron diffraction coupled to TEM may help to assign a given composition to a certain morphology. In our case, we can attribute a composition to most oxygen-bearing objects, regardless of the crystallinity. To illustrate this, **Figure 10** shows a typical example. The overall spectrum of this sample presents features of superoxide (529 eV), peroxide (531 eV), and a component typical for fully oxidized oxygen, such as carbonate or hydroxide (533 eV). However, spectra at different points differ significantly, which implies that heterogeneity is larger than the spatial resolution, and that the spectral (and hence chemical) difference between the various independent components is remarkable. By inspecting differential images we can localize the spots where each component has maximum concentration. We can distinctly observe oblate particles with an essentially peroxide composition, probably corresponding to platelets reported in the literature [29]. Centering at the 533 eV peak some needle-like particles, but also a more diffuse background can be imaged. Local spectra strongly suggest a hydroxide-like composition. The weaker superoxide component cannot be localized at specific points. A very characteristic spectrum, that is not evident in the overall spectrum, is instead found in a few spots, and corresponds to ice, probably deposited during the transfer process. Even if this component is external to the cathode material, it shows that statistically less relevant components that do not appear in the total spectrum can be detected if spatially well localized. Thus, the fluctuating local spectra not only greatly facilitate the attribution of the components that appear mixed in the integrated spectrum, but even allow lowering the detection limit.
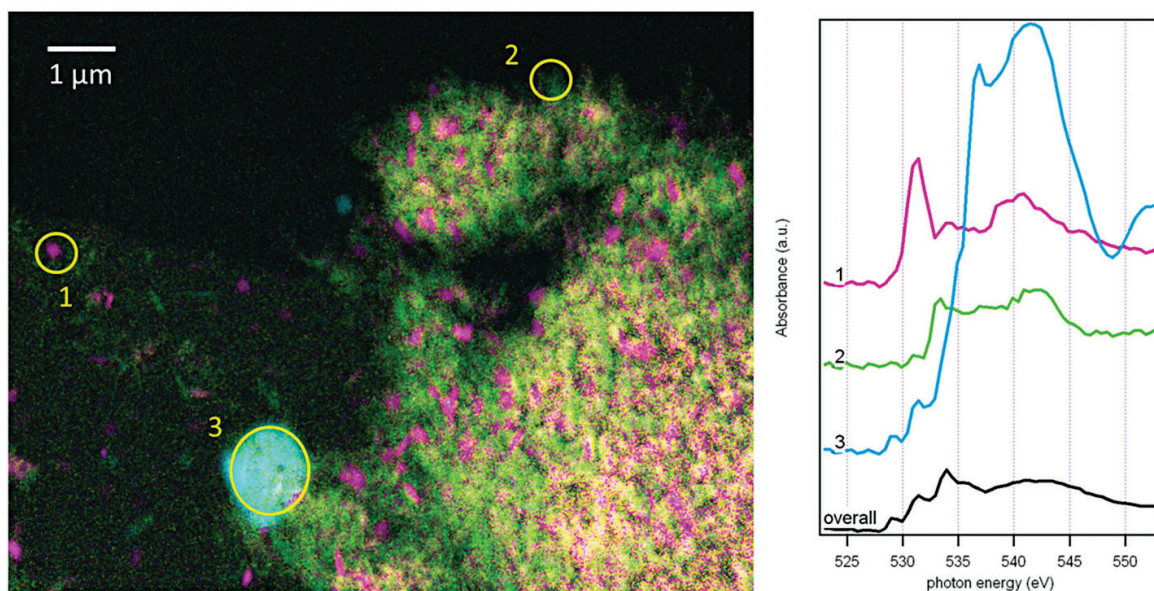

Figure 10. Left: Combination of differential images for different spectral components. Each component is represented with a respective color: superoxide (yellow), peroxide (magenta), hydroxide (green), and ice (cyan). Right: Absorption spectra in the O K region at selected points and for the overall image.

5.2. Toroidal particles

The sample reported in **Figure 11** includes the characteristic toroidal-shaped particles also reported by several authors working with ether-based solvents. Beside these main objects, we actually also appreciate platelet-like particles and irregular aggregates. Also in this case, differently shaped particles present different composition. Small platelets and irregular particle aggregates are mainly composed of carbonate (red). Instead, Li superoxide and peroxide dominate in toroidal objects (green). From intensity maps, it is also possible to generate ratio or fraction maps that are useful to tell if some components are associated.

Such estimations indicate that toroidal peroxide particles included 10–30% superoxide-like phases. Superoxide does not appear to show any preferential localization with respect to peroxide in the particles, suggesting some coprecipitation mechanism that may favor toroid formation. In fact, smaller particles have smaller superoxide content than large particles. Significant amount of carbonates were found irregularly distributed on the electrode, appearing as aggregates, but also coating lithium peroxide particles. A closer analysis suggests that carbonates form a shell on the surface of all particles, so that smaller particles seem associated to relatively larger quantities of carbonate. This resembles a passivating layer, indicating that carbonate formation is a surface reaction and forms a kind of passivating layer. Thus, a strategy for more reversible batteries appears to be conditions that favor operation with larger particles.

5.3. Redox mediators and recharge

The use of redox mediators has opened an important strategy to recharge lithium-oxygen batteries [30]. These are redox-active soluble molecules, which are able to readily oxidize electrochemically during charge, and then reach the peroxide deposits giving place to a chemical redox reaction that evolves oxygen and switches back the molecule to its reduced state. By providing alternative electron paths from the insulating peroxide to the electrode collector, they act as catalysts, with considerable decrease of overpotentials increased charging rates and efficiencies. One of the requirements for the mediator is its stability to the electrochemical conditions, in effect we found UV-visible spectroscopy evidence that oxygen actually reacts with the mediator iodide [31]. Other authors instead have shown that the product may also be significantly affected by iodide [32]. By comparing **Figure 12** with **Figure 11** we could not notice any remarkable difference in the morphology or composition of fully discharged electrodes with or without iodide. Although in this case it is difficult to unambiguously detect subtle spectral changes that may prove small deviations in the irreversible processes, the information we obtain is more representative of the relative amounts of oxygen in different chemical states. This allows affirming. That overall the mediator iodine has practically no effect on the proportions of main and side Li/O_2 discharge products. When we eventually recharge the battery, using these small TEM grid-based electrodes, the voltage usually increases fast above 4 V vs. Li. With the iodide mediator we instead obtain a large charge profile (**Figure 12a**). During this profile, we can observe that toroids disappear fast (sample B). Then, we can see that the sample just shows circular imprints inside a carbonate-like material at the place of the toroids (sample C). The spectrum still shows some peroxide,

in agreement with the tiny yellow fragments that can be noted embedded in the carbonate matrix, without being accessible even to the mediators, making the corresponding capacity highly irreversible.
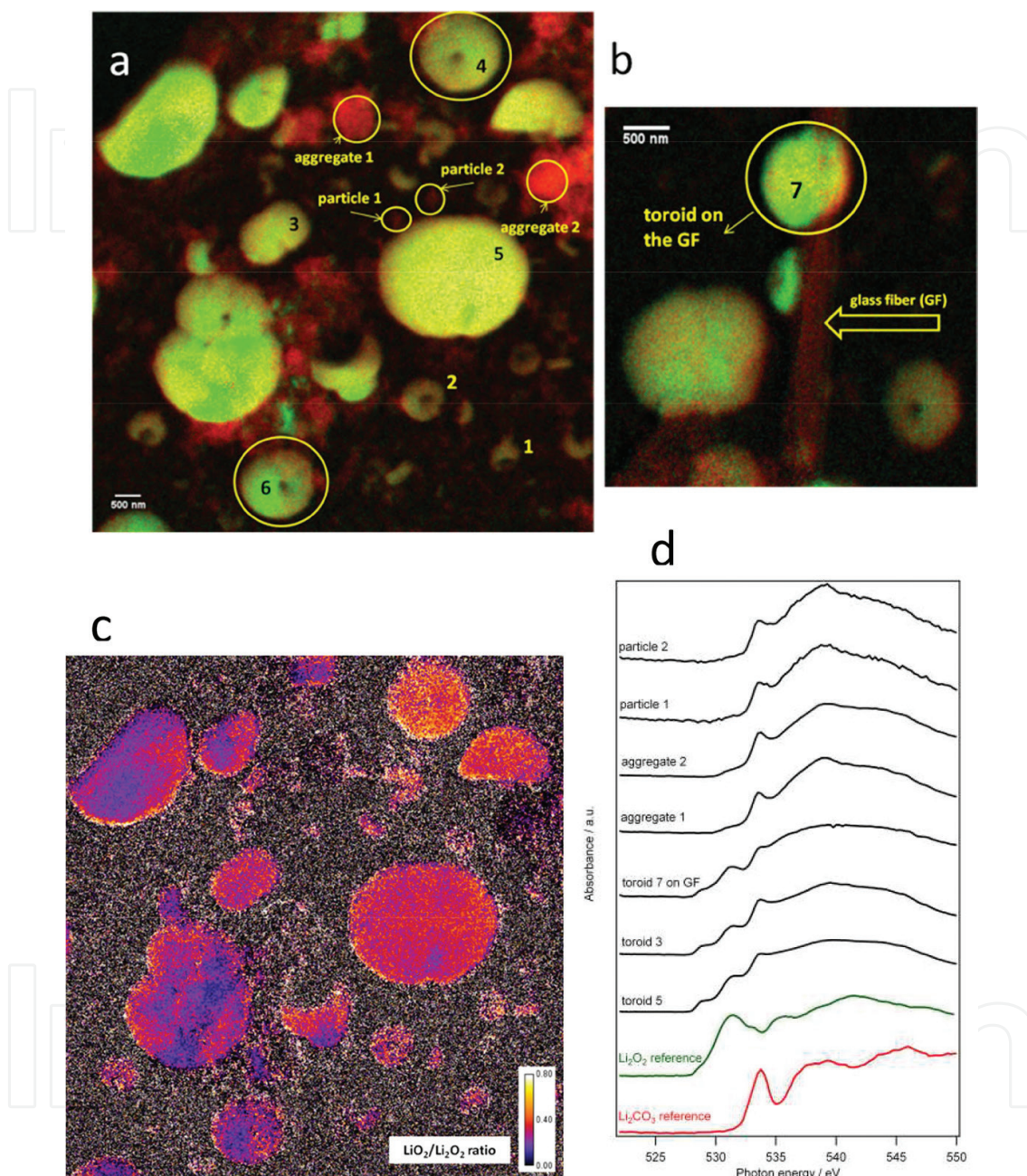

Figure 11. (a and b) TXM images of a carbon-coated Au TEM grid after being fully discharged in a Li-O_2 cell. The images are the result of overlapping three color maps with intensities proportional to the amounts of Li superoxide (cyan), Li peroxide (green), and carbonate (red). (c) Map of the LiO_2/Li_2O_2 ratio. The respective LiO_2 and Li_2O_2 intensities have been obtained by the same method. The gray noisy area results from regions with low LiO_2 and Li_2O_2 values. (d) Corresponding O K-edge XANES spectra at the selected points indicated by arrows in figures a and b, together with reference Li_2O_2 and Li_2CO_3 spectra. Reprinted with permission from Olivares-Marín et al. [11]. Copyright 2015 American Chemical Society.
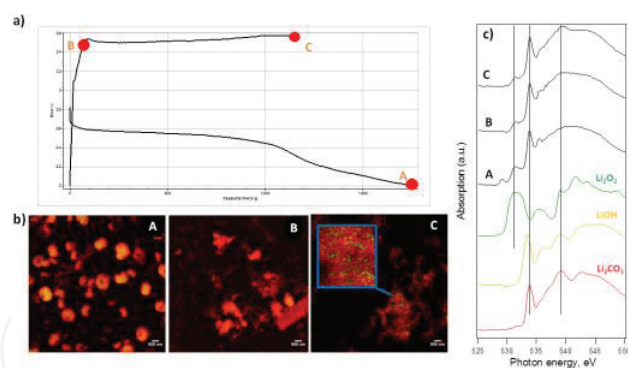
Figure 12. Galvanostatic discharge-charge profile of a TEM mesh-based cathode in a 1 M Li triflate electrolyte in TEGDME with a 0.02 M LiI additive (a), showing the position of three different samples. TXM images of the three samples (b) and corresponding overall O K spectra compared with references (c).

6. Conclusions

Full-field transmission soft X-ray microscopy is a powerful tool for the characterization of nanocomposites and nanostructured materials. Its high energy and space resolution provide accurate and semiquantitative chemical information at the scale of few tens of nm. This technique is particularly useful to inspect heterogeneities in all those materials involving the redox activity of several elements, including O and N. The unique access to the oxygen chemical state is extremely valuable to the investigation of metal air batteries. In this field, the technique contributes to understand the morphology and nature of the discharge products, their formation, and removal mechanism during discharge and charge of metal-air batteries. In particular, it is likely the most effective technique in detecting the critical superoxide component and its interplay with the other compounds present. The correlation between the respective spatial distributions gives one of the most comprehensive pictures of the reactivity and failure mechanisms, which hopefully will lead to strategies able to turn the Li/O_2 and other metal-air chemistries into a technological reality.

Acknowledgements

Author details

Dino Tonti[1]*, Mara Olivares-Marín[2], Andrea Sorrentino[3] and Eva Pereiro[3]

*Address all correspondence to: dino.t@csic.es

1 Institute of Materials Science of Barcelona, Spanish National Research Council (ICMAB-CSIC), Barcelona, Spain

2 CUM - University of Extremadura, Mérida, Spain

3 ALBA Synchrotron Light Source, MISTRAL Beamline – Experiments Division, Barcelona, Spain

References

[1]   Luntz AC, McCloskey BD. Nonaqueous Li-air batteries: a status report. Chem Rev. 2014;114(23):11721–50.

[2]   Christensen J, Albertus P, Sanchez-Carrera RS, Lohmann T, Kozinsky B, Liedtke R, et al. A Critical Review of Li/Air Batteries. J Electrochem Soc. 2012;159(2):R1–30.

[3]   Yao X, Dong Q, Cheng Q, Wang D. Why do lithium-oxygen batteries fail: parasitic chemical reactions and their synergistic effect. Angewandte Chemie - International Edition. 2016;55(38):11344–53.

[4]   Aurbach D, McCloskey BD, Nazar LF, Bruce PG. Advances in understanding mechanisms underpinning lithium–air batteries. Nat Energy. 2016;1(9):16128.

[5]   Aklalouch M, Olivares-Marín M, Lee RC, Palomino P, Enciso E, Tonti D. Mass-transport control on the discharge mechanism in Li-O_2 batteries using carbon cathodes with varied porosity. ChemSusChem. 2015;8(20):3465–71.

[6]   Gallant BM, Kwabi DG, Mitchell RR, Zhou J, Thompson CV, Shao-Horn Y. Influence of Li2O2 morphology on oxygen reduction and evolution kinetics in Li-O2 batteries. Energy Environ Sci. 2013;6(8):2518–28.

[7]   Elia GA, Hassoun J, Kwak WJ, Sun YK, Scrosati B, Mueller F, et al. An advanced lithium-air battery exploiting an ionic liquid-based electrolyte. Nano Lett. 2014;14(11):6572–7.

[8]   Yang J, Zhai D, Wang HH, Lau KC, Schlueter JA, Du P, et al. Evidence for lithium superoxide-like species in the discharge product of a Li-O2 battery. Phys Chem Chem Phys. 2013;15(11):3764–71.

[9]   Frith JT, Russell AE, Garcia-Araez N, Owen JR. An in-situ Raman study of the oxygen reduction reaction in ionic liquids. Electrochem Commun. 2014;46:33–5.

[10]   Zhai D, Lau KC, Wang HH, Wen J, Miller DJ, Lu J, et al. Interfacial effects on lithium superoxide disproportionation in Li-O2 batteries. Nano Lett. 2015;15(2):1041–6.

[11] Olivares-Marín M, Sorrentino A, Lee R-C, Pereiro E, Wu N-L, Tonti D. Spatial distribu-
      tions of discharged products of lithium–oxygen batteries revealed by synchrotron X-ray
      transmission microscopy. Nano Lett. 2015;15(10):6932–8

[12] Lu J, Lee YJ, Luo X, Lau KC, Asadi M, Wang HH, et al. A lithium-oxygen battery based
      on lithium superoxide. Nature. 2016;529(7586):377–82.

[13] Bender CL, Hartmann P, Vračar M, Adelhelm P, Janek J. On the thermodynamics, the
      role of the carbon cathode, and the cycle life of the sodium superoxide (NaO2) battery.
      Adv Energy Mater. 2014;4(12):1301863.

[14] Ren X, Wu Y. A low-overpotential potassium-oxygen battery based on potassium
      superoxide. J Am Chem Soc. 2013;135(8):2923–6.

[15] Zhang Y, Cui Q, Zhang X, McKee WC, Xu Y, Ling S, et al. Amorphous Li2O2: chemical
      synthesis and electrochemical properties. Angewandte Chemie - International Edition.
      2016;55(36):10717–21.

[16] Attwood D. Soft X-Rays and Extreme Ultraviolet Radiation: Principles and Applications.
      Cambridge: Cambridge University Press; 1999, 1999/008/28.

[17] Mobilio S. Interaction between radiation and matter: an introduction. In: Mobilio S, Vlaic G,
      editors. Synchrotron Radiation: Fundamentals, Methodologies and Applications. Vol. 82.
      Bologna: Società Italiana di Fisica; 2001.

[18] Pereiro E, Nicolas J, Ferrer S, Howells MR. A soft X-ray beamline for transmission X-ray
      microscopy at ALBA. J Synchrotron Radiat. 2009;16(Pt 4):505–12.

[19] Sorrentino A, Nicolás J, Valcárcel R, Chichón FJ, Rosanes M, Avila J, et al. MISTRAL: a
      transmission soft X-ray microscopy beamline for cryo nano-tomography of biological
      samples and magnetic domains imaging. J Synchrot Radiat. 2015;22(4):1112–7.

[20] Chao WL, Harteneck BD, Liddle JA, Anderson EH, Attwood DT. Soft X-ray microscopy
      at a spatial resolution better than 15 nm. Nature. 2005;435(7046):1210–3.

[21] Sayre D, Kirz J, Feder R, Kim DM, Spiller E. Potential operating region for ultrasoft X-ray
      microscopy of biological-materials. Science. 1977;196(4296):1339–40.

[22] Cazaux J. A physical approach to the radiation damage mechanisms induced by X-rays
      in X-ray microscopy and related techniques. J Microscopy-Oxford. 1997;188:106–24.

[23] Olivares-Marín M, Palomino P, Amarilla JM, Enciso E, Tonti D. Effects of architecture
      on the electrochemistry of binder-free inverse opal carbons as Li-air cathodes in an ionic
      liquid-based electrolyte. J Mat Chem A. 2013;1(45):14270–9.

[24] Qiao R, Chuang YD, Yan S, Yang W. Soft x-ray irradiation effects of Li(2)O(2), Li(2)CO(3)
      and Li(2)O revealed by absorption spectroscopy. PLoS One. 2012;7(11):e49182.

[25] Black R, Oh SH, Lee JH, Yim T, Adams B, Nazar LF. Screening for superoxide reactivity in
      Li-O-2 batteries: effect on Li2O2/LiOH crystallization. J Am Chem Soc. 2012;134(6):2902–5.

[26] Ruckman MW, Chen J, Qiu SL, Kuiper P, Strongin M, Dunlap BI. Interpreting the near Edges of O2 and O2- in alkali-metal superoxides. Phys Rev Lett. 1991;67(18):2533–6.

[27] Kremer JR, Mastronarde DN, McIntosh JR. Computer visualization of three-dimensional image data using IMOD. J Struct Biol. 1996;116(1):71–6.

[28] Jaumot J, Gargallo R, de Juan A, Tauler R. A graphical user-friendly interface for MCR-ALS: a new tool for multivariate curve resolution in MATLAB. Chemomet Intell Lab Syst. 2005;76(1):101–10.

[29] Zakharchenko TK, Kozmenkova AY, Itkis DM, Goodilin EA. Lithium peroxide crystal clusters as a natural growth feature of discharge products in Li-O2 cells. Beilstein J Nanotechnol. 2013;4(1):758–62.

[30] Chen Y, Freunberger SA, Peng Z, Fontaine O, Bruce PG. Charging a Li-O2 battery using a redox mediator. Nat Chem. 2013;5(6):489–94.

[31] Landa-Medrano I, Olivares-Marín M, Pinedo R, Ruiz de Larramendi I, Rojo T, Tonti D. Operando UV-visible spectroscopy evidence of the reactions of iodide as redox mediator in Li–O2 batteries. Electrochem Commun. 2015;59:24–7.

[32] Kwak W-J, Hirshberg D, Sharon D, Shin H-J, Afri M, Park J-B, et al. Understanding the behavior of Li–oxygen cells containing LiI. J Mater Chem A. 2015;3(16):8855–64.